Research in the Mathematical Sciences manuscript No.
(will be inserted by the editor)

Initial Investigations of Precipitating Quasi-Geostrophic Turbulence with Phase Changes

Rentian Hu · Thomas K. Edwards · Leslie M. Smith · Samuel N. Stechmann

Submitted: June 1, 2020
Revised: October 30, 2020

Abstract Asymptotic models have provided valuable insight into the atmosphere and its dynamics. Nevertheless, one shortcoming of the classic asymptotic models, such as the quasi-geostrophic (QG) equations, is that they describe a "dry" atmosphere and do not account for water vapor, clouds, and rainfall. Recently, precipitating QG (PQG) equations were derived in an asymptotic limit, starting from atmospheric equations that include changes of water between different phases (vapor, liquid, etc.). The PQG equations include Heaviside nonlinearities due to phase changes, which can potentially have a significant influence on QG turbulence. Here, simple numerical methods are presented for the PQG equations, accounting for the Heaviside nonlinearities, and an initial set of numerical experiments is conducted to probe the behavior of PQG turbulence. A two-vertical-level setup is used for an idealized vertical structure, as in the classic Phillips model. Due to phase changes and rainfall, the midlatitude jet variability displays a variety of behaviors, including poleward propagation of the latitude of the jet. The simulations suggest a new set

Rentian Hu
Department of Mathematics, University of Wisconsin–Madison
E-mail: rhu29@wisc.edu

Thomas K. Edwards
Department of Mathematics, University of Wisconsin–Madison

Leslie M. Smith
Department of Mathematics, and Department of Engineering Physics, University of Wisconsin–Madison

Samuel N. Stechmann
Department of Mathematics, and Department of Atmospheric and Oceanic Sciences, University of Wisconsin–Madison

of phenomena that arise in QG turbulence due to phase changes, in a simplified model that is potentially amenable to mathematical analysis.

Keywords geophysical fluid dynamics · partial differential equations · numerical simulation · discontinuous coefficients · interface

PACS 02.60.Cb · 02.30.Jr · 02.70.-c · 47.11.-j

Mathematics Subject Classification (2010) 65M22 · 35M10 · 86-08

1 Introduction

The dynamics of the atmosphere is complicated, and one avenue for obtaining basic understanding has been asymptotic models. Among a variety of classic asymptotic models, one of the most useful has been the quasi-geostrophic (QG) limit [46,76]. The QG approximation has been used for some of our fundamental knowledge of many atmospheric phenomena, such as baroclinic instability and geostrophic turbulence [5,6,64,7,67,69,63,46,76,72], and it provides insights that have been used in practical applications of data assimilation and weather prediction [27].

While the QG approximation has been invaluable, one limitation of the classical theory is that it is a "dry" theory—i.e., it describes the "dry" atmospheric quantities of velocity, pressure, temperature, etc., but it does not describe water vapor, clouds, and rainfall. To extend the classic dry theory, a variety of approaches have been used to include moisture, latent heating, etc. [4,16,38]. While these extensions have provided new insights into the effects of moisture, latent heating, etc., they tend to treat moisture somewhat as an add-on rather than as an integral part of the system.

Recently, a moist QG theory was derived by starting from the equations for a moist atmosphere, including moisture from the start and on equal footing with the dry variables [70]. These precipitating QG (PQG) equations are a set of new partial differential equations (PDEs) that involve Heaviside nonlinearities due to phase changes of water (between phases of vapor, liquid, etc.). Like the classic QG equations, the PQG equations involve both transport PDEs and an elliptic PDE. A new feature of the PQG equations is that the elliptic PDE is nonlinear instead of linear, and it has discontinuous coefficients.

The main purpose of the present paper is to describe an initial investigation of PQG turbulence. Countless questions could be asked about a precipitating version of QG turbulence, beyond the classic case of dry QG turbulence. For instance, one set of questions could focus on the effects of moisture and phase changes on geostrophic turbulence, in comparison to dry geostrophic turbulence. Another set of questions could focus on the effects of the various new parameters that arise in the moist case (evaporation rate, meridional moisture gradient, etc.), and the sensitivity of the turbulence to changes in these moist parameters. It would also be interesting to compare PQG turbulence with geostrophic turbulence in nature or in more comprehensive models [19], although we leave a detailed comparison for future work and focus here on QG

equations in this initial investigation. With these types of questions in mind, one goal here is to describe some of the new behavior that arises in PQG turbulence, and, in order to do so, we also describe a numerical method for simulating PQG dynamics, with the goal of incorporating the Heaviside nonlinearities in a numerical framework that is as simple as possible and as close as possible to the methods typically used for the dry QG equations. In this spirit of considering simple scenarios for initial investigations, we also focus here on the two-level QG equations and leave an investigation of three-dimensional PQG dynamics for future work.

The present work adds to a small set of prior studies on the PQG equations. The only two PQG investigations that have involved phase changes are the original derivation [70], which also included an example solution of the nonlinear elliptic PDE, and an investigation of discontinuous front solutions [78]. Another set of studies investigated PQG equations with precipitation but without phase changes, in which case some analytical theory is made possible in the absence of the Heaviside nonlinearities. These studies investigated linear baroclinic instability and the effects of precipitation on moisture transport [77], and two investigations of geostrophic turbulence, one with a focus on water spectra [15] and another with a focus on coherent corridors of water that resemble atmospheric rivers [14]. The present work on PQG turbulence is distinguished by its inclusion of phase changes and associated Heaviside nonlinearities. In a related body of work, the PQG dynamical equations were not directly used, but the PQG asymptotics motivated methods for decompositions into balanced and unbalanced components, using a new type of potential vorticity inversion that incorporates moisture and phase changes [79,80].

The present paper also contributes to the small body of work on QG turbulence in the presence of moisture. One paper has examined moist QG turbulence in an idealized setting [38], in a square domain with doubly periodic boundary conditions, similar to the setup of the present paper. A more realistic, global setting on a sphere has also been used in some studies of moist QG turbulence [60,37]. One difference from the present paper is in the treatment of precipitation and latent heat release. Here, a large-scale saturation condition is used, which is inherited from the underlying, more comprehensive models of cloud microphysics, and no convective parameterization is included; in contrast, the other moist QG models [38,60,37] use a parameterization of small-scale convection rather than a large-scale saturation condition. While it would be interesting to combine both treatments (i.e., both large-scale saturation/condensation and convective parameterization), here we focus only on the large-scale saturation as the newer aspect of moist QG turbulence.

This article is dedicated to Andrew J. Majda to celebrate his 70th birthday. He has had an enormous influence on the present authors, and we are grateful for his collaboration and friendship. A vast amount of his work has influenced the present paper, including work on geophysical fluid dynamics, quasi-geostrophic equations, partial differential equations, singular limits, fast-wave averaging for fluids with small Mach, Froude, and/or Rossby numbers [34,35,43,17,18,47,46,48,44,53,45,11,12,13,49], moist atmospheric

dynamics, [20,28,29,31,30,36,71,52,51,54,10,32] and numerical and/or statistical methods using the quasi-geostrophic equations as a test model [1,2,22,23,21,24,39,65,66,50].

The remainder of the paper is organized as follows. The PQG equations are described in section 2, along with a description of the numerical methods, including the treatment of the Heaviside nonlinearities. In section 3, a suite of numerical simulations is presented, and a main highlight is that phase changes cause the jet stream to propagate poleward. Also discussed is the smoothness—or lack thereof—of the various model variables, as a result of the discontinuous coefficients from phase changes. Finally, conclusions and future directions are discussed in section 4.

2 Model description

In this section, we describe the PDEs of the PQG model, and the energy principle. One new aspect here is the setup of a version of the model with only two vertical levels. Such a setup is valuable because it essentially turns a three-dimensional (3D) problem in (x, y, z) into a two-dimensional (2D) problem in (x, y), at a substantial computational savings; yet it arguably contains the most essential physics, including both a barotropic (height-independent) mode and a baroclinic mode. As such, the two-level setup has been valuable in past studies of QG equations [64,38,76,72,65]. Some subtleties arise in moving from 3D to 2D here, due to precipitation, and they are discussed below. An energy principle suggests that the 2D model has firm mathematical and physical grounding. Finally, a numerical method is proposed at the end of the section. A new aspect of the numerical method, in comparison to dry QG models, is the need to handle discontinuous coefficients associated with phase changes.

2.1 Two-level PQG equations

To obtain a two-level version of the PQG equations, we start with description of the three-dimensional PQG equations. Details of derivation of the PQG equations can be found in [70]. The 3D evolution equations can be written in the following nondimensional form:

$$\frac{\mathrm{D}_h \zeta}{\mathrm{D}t} + \beta v = \frac{\partial w}{\partial z} \tag{1a}$$

$$\frac{\mathrm{D}_h \theta_e}{\mathrm{D}t} + w \frac{L_{ds}}{L_{du}} \frac{L_{ds}}{L} = 0 \tag{1b}$$

$$\frac{\mathrm{D}_h q_t}{\mathrm{D}t} - w G_M \frac{L_{ds}}{L_{du}} \frac{L_{ds}}{L} = V_r \frac{\partial q_r}{\partial z} \tag{1c}$$

where $\zeta(\mathbf{x}, t), \theta_e(\mathbf{x}, t), q_t(\mathbf{x}, t), q_r(\mathbf{x}, t)$ are three dimensional functions of $\mathbf{x} = (x, y, z)$ and time t; $\zeta = \partial_x v - \partial_y u$ is the vertical component of relative vorticity where $\mathbf{u} = (u, v, w)$ is the fluid velocity; β is the change in rotation rate

with respect to latitude; θ_e is the equivalent potential temperature; G_M is a nondimensional parameter defined to be $-\frac{L_v}{c_p}\frac{d\tilde{q}_t/dz}{d\tilde{\theta}_e/dz}$ where L_v is latent heat of vaporization, c_p is specific heat, and terms with tilde $(\tilde{q}_t, \tilde{\theta}_e)$ are background values of the corresponding variables that only depend on the height z; L is a reference length scale; L_{ds} is the (saturated) Rossby radius of deformation; L_{du} is the (unsaturated) Rossby radius of deformation. The two Rossby radii of deformation, L_{du} and L_{ds}, are related to the background profiles $\tilde{\theta}_e(z)$ and $\tilde{q}_t(z)$ [70], and they are related to the parameter G_M via the relation

$$\left(\frac{L_{du}}{L_{ds}}\right)^2 = 1 + G_M$$

which shows that it is sufficient to specify only two of the three parameters L_{du}, L_{ds}, and G_M; q_t is the mixing ratio of total water; V_r is the (nondimensional) fall speed of rain, taken to be constant. Also, the material derivative at horizontal level is $\frac{\mathrm{D}_h}{\mathrm{D}t}(\cdot) = \partial_t(\cdot) + \mathbf{u}_h \cdot \nabla_h$. The variable q_r is the mixing ratio of rainwater, and it is defined diagnostically as $q_r = \max(0, q_t - q_{vs})$, i.e., as the amount of water above saturation, where q_{vs} is the saturation mixing ratio. This max function for defining q_r is one place where phase changes enter the equations; other appearances of phase change nonlinearities will be noted below.

We then define two quantities: the potential vorticity PV_e and a moist variable M:

$$PV_e = \zeta + \frac{L_{du}}{L_{ds}}\frac{L}{L_{ds}}\frac{\partial \theta_e}{\partial z} \tag{2a}$$

$$M = q_t + G_M \theta_e \tag{2b}$$

The motivation for using PV_e and M is that they eliminate w from (1). Their evolution equation can be found from (1) and (2) to be

$$\frac{\mathrm{D}_h PV_e}{\mathrm{D}t} + \beta v = -\frac{L_{du}}{L_{ds}}\frac{L}{L_{ds}}\frac{\partial \mathbf{u}_h}{\partial z} \cdot \nabla_h \theta_e \tag{3a}$$

$$\frac{\mathrm{D}_h M}{\mathrm{D}t} = V_r \frac{\partial}{\partial z} q_r. \tag{3b}$$

Note that, in terms of the new quantity M, the rainwater $q_r = \max(0, q_t - q_{vs})$ can be written as $q_r = \max(0, M - G_M\theta_e - q_{vs})$.

To close the system, additional diagnostic relations are needed. In particular, in order to evolve the prognostic variables PV_e and M in (3), one also needs $\mathbf{u}_h = (u, v)$, θ_e, and q_r. To find these additional variables, the definitions of PV_e and M in (2) are inverted by turning them into the elliptic PDE

$$\nabla_h^2 \psi + \frac{L_{du}}{L_{ds}}\frac{L}{L_{ds}}\frac{\partial}{\partial z}\left[H_u \theta_{eu}(\psi_z, M, z) + H_s \theta_{es}(\psi_z, M, z)\right] = PV_e. \tag{4}$$

This PDE arises from (2) by noting that the relative vorticity and streamfunction are related by $\zeta = \nabla_h^2 \psi$, and by defining θ_e using different functions in different phases, which are explained further below. Upon writing out the

functions $\theta_{eu}(\psi_z, M, z)$ and $\theta_{es}(\psi_z, M, z)$ that define θ_e in unsaturated and saturated phases, respectively, the elliptic PDE becomes

$$\nabla_h^2\psi + \frac{\partial}{\partial z}\left[H_s\left(\frac{L^2}{L_{ds}^2}\frac{\partial\psi}{\partial z} + \frac{L_{du}}{L_{ds}}\frac{L}{L_{ds}}q_{vs}\right) + H_u\left(\frac{L^2}{L_{du}^2}\frac{\partial\psi}{\partial z} + \frac{L}{L_{du}}M\right)\right] = PV_e. \tag{5}$$

Note two properties of this elliptic PDE: (i) it has discontinuous coefficients, due to the Heaviside functions H_u and H_s, and (ii) it is nonlinear, since the Heavisides are functions of q_t, which itself is a function of ψ_z, as explained further below. By solving this elliptic PDE, given knowledge of PV_e and M, one obtains the streamfunction ψ, from which all other variables can be found. For instance, from the leading order of the asymptotic derivation, the geostrophic balance and hydrostatic balance conditions are:

$$\mathbf{u}_h = \nabla_h^\perp\psi, \quad \theta = \frac{L}{L_{du}}\frac{\partial\psi}{\partial z} \tag{6}$$

where θ is the potential temperature, and $\nabla_h^\perp = (-\partial_y, \partial_x)$. These balance conditions provide the definitions of θ and the velocity variables u and v, given streamfunction ψ.

Phase changes appear in two places above: in the definition of $q_r = \max(0, q_t - q_{vs})$, and via the equivalent potential temperature θ_e in (4)–(5). The following relations are useful for defining and relating the different variables and the Heaviside functions. The equivalent potential temperature θ_e can be defined in terms of the potential temperature θ and q_t as

$$\theta_e = (\theta + q_t)H_u + (\theta + q_{vs})H_s, \tag{7}$$

where a different formula is used in different phases [70]. Also, q_t can be defined in terms of M and θ_e, from (2b), as $q_t = M - G_M\theta_e$; it follows from (7) that q_t can be defined in terms of M and θ as

$$q_t = \frac{M - G_M\theta}{1 + G_M}H_u + (M - G_M\theta - G_M q_{vs})H_s. \tag{8}$$

Here, the Heaviside functions H_u and H_s are indicators of the unsaturated and saturated phases, respectively. The saturated phase ($H_s = 1$) is defined as the region where total water q_t is above the saturation value:

$$H_s = H(q_t - q_{vs}), \qquad H_u = 1 - H_s, \tag{9}$$

where $H(x)$ is a Heaviside function that equals 0 for $x < 0$ and 1 for $x > 0$.

A rigid lid boundary condition $w = 0$ is imposed at top and bottom. The vertical boundary condition of the nondimensional form of PQG equations (1) thus becomes

$$w = 0, \quad \frac{\mathrm{D}_h\theta_e}{\mathrm{D}t} = 0, \quad \frac{\mathrm{D}_h q_t}{\mathrm{D}t} = V_r\frac{\partial q_r}{\partial z} \tag{10}$$

on both top and bottom [15]. As a further simplification, one could choose initial conditions with $\theta_e = 0$ and $q_t = 0$ on the domain top. As a result, due

to the boundary evolution in (10), θ_e and q_t would remain 0 at the domain top for all times:

$$w = 0, \quad \theta_e = 0, \quad q_t = 0, \quad \text{at top boundary.} \tag{11}$$

In attempting a similar simplification at the bottom boundary, $\theta_e = 0$ could be used by similar reasoning, but a complication arises due to precipitation. In particular, if q_t is initially 0 at the bottom boundary, it may not remain 0 for all times, since the precipitation term $V_r \partial q_r / \partial z$ can transport water from the interior of the domain to the bottom boundary. This is the main subtlety that arises here in moving from the 3D system to a simplified two-level system, and in seeking a setup without boundary dynamics. One approach would be to include an evolution equation for the bottom boundary values of q_t, as in (10); however, the coupling of boundary dynamics and interior dynamics can bring nontrivial challenges for QG systems [74,73]. Since the present goal is to explore the simplest possible setup with two vertical levels, we will set all thermodynamics variables to zero at the bottom boundary for all times:

$$w = 0, \quad \theta_e = 0, \quad q_t = 0, \quad \text{at bottom boundary.} \tag{12}$$

While the $q_t = 0$ condition does not directly follow from the $w = 0$ boundary condition in a precipitating system, it is at least approximately valid if precipitation covers a small fraction of the domain, as is typically the case for the real atmosphere. Also, it is shown below that the system still retains an energy principle, which suggests this simplified setup has a firm mathematical and physical foundation.

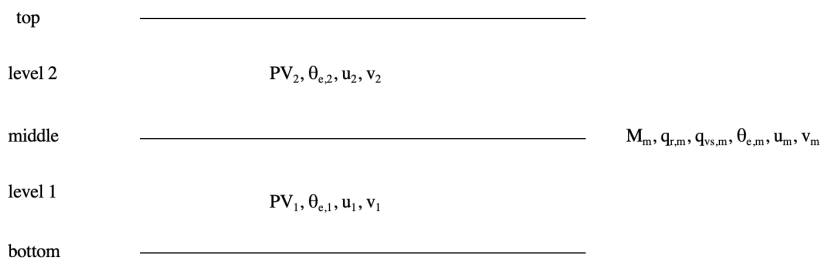

Fig. 1 Diagram of the two level set-up

After here, the two-level version of the PQG equations can be deduced. The move to the two-level version is similar to what is done in the dry case, although the subtlety described above, due to precipitation effects at the bottom boundary, should be noted. A staggered grid is used in the vertical direction,

as shown in Figure 1. The domain height is $2\Delta z$ for a setup with two vertical levels. The velocity is defined on two interior levels, denoted as levels 1 and 2, and located at heights of $\Delta z/2$ and $3\Delta z/2$, respectively. The thermodynamic variables are defined on domain top, domain bottom, and the middle of the domain (denoted by a subscript "m"). Subscripts of 1, 2, and m are used to indicate the material derivative at each level: $\frac{\mathrm{D}_1}{\mathrm{D}t}(\cdot) = \partial_t(\cdot) + u_1\partial_x(\cdot) + v_1\partial_y(\cdot)$, and similarly for $\frac{\mathrm{D}_2}{\mathrm{D}t}(\cdot)$ and $\frac{\mathrm{D}_m}{\mathrm{D}t}(\cdot)$. The two-level equations are then obtained from (3) by using centered finite differences in z and the boundary conditions in (11)–(12). The two level version of the PQG equations is then:

$$\frac{\mathrm{D}_1 PV_1}{\mathrm{D}t} + \beta v_1 = -\frac{L_{du}}{L_{ds}}\frac{L}{L_{ds}}\frac{\partial \mathbf{u}_h}{\partial z}\cdot\nabla_h\theta_{e,1} \tag{13a}$$

$$\frac{\mathrm{D}_2 PV_2}{\mathrm{D}t} + \beta v_2 = -\frac{L_{du}}{L_{ds}}\frac{L}{L_{ds}}\frac{\partial \mathbf{u}_h}{\partial z}\cdot\nabla_h\theta_{e,2} \tag{13b}$$

$$\frac{\mathrm{D}_m M_m}{\mathrm{D}t} = -\frac{V_r}{\Delta z}q_{r,m} \tag{13c}$$

with

$$\begin{aligned} PV_{e,1} = \nabla_h^2\psi_1 &+ H_s\left(\left(\frac{L}{L_{ds}}\frac{1}{\Delta z}\right)^2(\psi_2-\psi_1) + \frac{L_{du}}{L_{ds}}\frac{L}{L_{ds}}\frac{1}{\Delta z}q_{vs,m}\right) \\ &+ H_u\left(\left(\frac{L}{L_{du}}\frac{1}{\Delta z}\right)^2(\psi_2-\psi_1) + \frac{L}{L_{du}}\frac{1}{\Delta z}M_m\right) \end{aligned} \tag{14a}$$

$$\begin{aligned} PV_{e,2} = \nabla_h^2\psi_2 &+ H_s\left(\left(\frac{L}{L_{ds}}\frac{1}{\Delta z}\right)^2(\psi_1-\psi_2) - \frac{L_{du}}{L_{ds}}\frac{L}{L_{ds}}\frac{1}{\Delta z}q_{vs,m}\right) \\ &+ H_u\left(\left(\frac{L}{L_{du}}\frac{1}{\Delta z}\right)^2(\psi_1-\psi_2) - \frac{L}{L_{du}}\frac{1}{\Delta z}M_m\right) \end{aligned} \tag{14b}$$

$$\theta_{e,m} = H_s\left(\frac{L}{L_{du}}\frac{\psi_2-\psi_1}{\Delta z} + q_{vs}\right) + \frac{1}{1+G_M}\left(H_u\frac{L}{L_{du}}\frac{\psi_2-\psi_1}{\Delta z} + H_u M_m\right) \tag{14c}$$

$$q_{t,m} = M_m - G_M\theta_{e,m} \tag{14d}$$

$$q_{r,m} = \max(0, q_{t,m} - q_{vs,m}) \tag{14e}$$

$$q_{vs,m} = q_{vs}^0 + q_{vs}^1\theta_m \tag{14f}$$

$$u_i = -\frac{\partial\psi_i}{\partial y} \text{ for } i = 1,2 \tag{14g}$$

$$v_i = \frac{\partial\psi_i}{\partial x} \text{ for } i = 1,2 \tag{14h}$$

Note that the term $\partial\mathbf{u}_h/\partial z$ was left written as a function of a continuum z coordinate in order to ease notation. It is actually defined using centered finite differences in the same way as the other terms above. (Recall Fig. 1 for an illustration of the staggered grid.) Explicitly, for instance, the value of

$\partial \mathbf{u}_h/\partial z$ at level 1 is defined as the average of $\partial \mathbf{u}_h/\partial z$ values at the mid-level (subscript m) and bottom boundary (subscript b), which are $(\mathbf{u}_2-\mathbf{u}_1)/\Delta z$ and 0, respectively, where a free-slip bottom boundary condition of $\partial \mathbf{u}_h/\partial z = 0$ is used, which follows from $\partial\psi/\partial z = 0$ from (6)–(12).

Also note that an upwind scheme was used to write $V_r \partial q_r/\partial z \approx (V_r/\Delta z)(q_r|_{z=z_T} - q_r|_{z=z_m})$ in (13c) at z_m. An upwind scheme is appropriate for this term since rain falls downward. Since $q_t = 0$ and $q_r = 0$ at $z = z_T$ for all times, it follows that $V_r \partial q_r/\partial z \approx -(V_r/\Delta z) q_{r,m}$.

An energy principle for the two-level system can be obtained by considering four contributions to the total energy: kinetic energy (KE), unsaturated potential energy (PE_u), saturated potential energy (PE_s), and a moist energy (ME). These four energy contributions are defined as

$$\begin{aligned} KE &= \frac{1}{2}\int_A |\nabla_h \psi_1|^2 + |\nabla_h \psi_2|^2 dA, \\ PE_u &= \frac{1}{2}\int_A H_u \frac{L^2}{L_{du}^2}\left(\frac{\psi_2-\psi_1}{\Delta z}\right)^2 dA, \\ PE_s &= \frac{1}{2}\int_A H_s \frac{L^2}{L_{ds}^2}\left(\frac{\psi_2-\psi_1}{\Delta z}\right)^2 dA, \\ ME &= \frac{1}{2}\int_A H_u \frac{1}{G_M}\left(M - \frac{L_{du}^2}{L_{ds}^2} q_{vs}\right)^2 dA, \end{aligned} \tag{15}$$

which are obtained from the 3D PQG energy [70] by applying finite differences in place of the vertical derivative $\partial/\partial z$.

The energy evolution can be found by taking a time derivative of each energy component:

$$\begin{aligned} \frac{d}{dt}KE &= \int_A w_m \frac{\psi_2-\psi_1}{\Delta z} dA \\ \frac{d}{dt}PE_u &= -\int_A H_u w_m \frac{\psi_2-\psi_1}{\Delta z} dA \\ &\quad - \frac{1}{2}\int_A \frac{\mathrm{D}_h H_s}{\mathrm{D}t}\frac{L^2}{L_{du}^2}\frac{(\psi_2-\psi_1)^2}{(\Delta z)^2} dA \\ \frac{d}{dt}PE_s &= -\int_A H_s w_m \frac{\psi_2-\psi_1}{\Delta z} dA \\ &\quad + \frac{1}{2}\int_A \frac{\mathrm{D}_h H_s}{\mathrm{D}t}\frac{L^2}{L_{ds}^2}\frac{(\psi_2-\psi_1)^2}{(\Delta z)^2} dA \\ \frac{d}{dt}ME &= \frac{1}{2}\int_A \frac{\mathrm{D}_h H_s}{\mathrm{D}t}\frac{(\psi_2-\psi_1)^2}{(\Delta z)^2}\left(\frac{L^2}{L_{du}^2} - \frac{L^2}{L_{ds}^2}\right) dA. \end{aligned} \tag{16}$$

The calculation of these time derivatives is described further in the appendix. It then follows that the total energy is conserved,

$$\frac{d}{dt}(KE + PE_u + PE_s + ME) = 0. \tag{17}$$

Note that energy is conserved, even though water can be lost from the interior of the domain due to precipitation. In more comprehensive systems, energy loss due to precipitation would arise from a hydrometeor drag term $-\rho g q_r$ in the buoyancy [61,62,25,26,55]. In the PQG system, however, the hydrometeor drag term is not a leading order term in the asymptotic derivation [70], so energy is conserved. It would be interesting in the future to retain hydrometeor drag as an additional small term which could dissipate energy on longer time scales.

2.2 Numerical methods and setup of numerical simulations

For numerical simulations, some additional features are added to the dynamical model in (13) to give

$$\frac{\mathrm{D}_1 PV_1}{\mathrm{D}t} - U\partial_x PV_1 + v_1 \partial_y PV_{1,bg} + \beta v_1 = -\frac{L_{du}}{L_{ds}}\frac{L}{L_{ds}}\frac{\partial \mathbf{u}_h}{\partial z}\cdot\nabla_h \theta_{e,1} - \kappa_M \Delta_h \psi_1 - \nu\Delta_h^4 PV_1 \tag{18a}$$

$$\frac{\mathrm{D}_2 PV_2}{\mathrm{D}t} + U\partial_x PV_2 + v_2 \partial_y PV_{2,bg} + \beta v_2 = -\frac{L_{du}}{L_{ds}}\frac{L}{L_{ds}}\frac{\partial \mathbf{u}_h}{\partial z}\cdot\nabla_h \theta_{e,2} - \nu\Delta_h^4 PV_2 \tag{18b}$$

$$\frac{\mathrm{D}_m M_m}{\mathrm{D}t} + v_m \partial_y M_{bg} = -\frac{V_r}{\Delta z} q_{r,m} - \nu\Delta_h^4 M_m + E. \tag{18c}$$

These equations now include an evaporation source term, E, and lower-level friction, represented by $-\kappa_M \Delta_h \psi_1$, where $\Delta_h = \nabla_h^2$ is the horizontal Laplacian operator. Also included are dissipation terms in the form of 4th-order hyperviscosity, represented by the operator $-\nu\Delta_h^4$. This setup is similar to other studies of two-level QG equations [65,15] although the present model also includes phase changes.

Note that equation (18) also splits the PV and M variables into background states and anomalies. The background values for PV and M are $PV_{j,bg} = (-1)^j(1 + q_{vs}^1)\frac{1}{(\Delta z)^2}\frac{L^2}{L_{ds}^2}(2Uy)$ and $M_{bg} = (Q_y + G_M \Theta_e)y$, where $\Theta_e y = (\Theta + Q_y)y$. Physically, Θy represents a meridional temperature gradient, which for $\Theta < 0$ corresponds to warmer air near the equator and colder air near the polar region. The vertical shear, U, is related to Θ as $\Theta y = -\frac{1}{\Delta z}\frac{L}{L_{du}}(2Uy)$, which follows from geostrophic and hydrostatic balance, (6). Also, Q_y represents a meridional gradient of water vapor, where, for $Q_y < 0$, more water vapor is present near the equator and less near the polar region. Finally, note that a constraint on the Θ and Q_y values arises, due to the threshold $q_{vs,m} = q_{vs}^0 + q_{vs}^1 \theta_m$ for the phase interface. More specifically, if this threshold formula is examined in the presence of a meridional gradient Θ, one can see that an inhomogeneity would be introduced, as $q_{vs,m}$ would also have a meridional gradient. To avoid the inhomogeneity, we impose the constraint $\partial_y(q_t - q_{vs}) = 0$, which will guarantee a homogeneous setup for the threshold, since the meridional gradient in the threshold q_{vs} is in balance with the meridional gradient in q_t. Such a constraint is needed here for a setup with

doubly periodic boundary conditions in the horizontal, as also implemented for a convective parameterization threshold in [38]. It follows from the constraint $\partial_y(q_t - q_{vs}) = 0$ that the meridional gradients of water vapor and potential temperature must be related by $Q_y = q^1_{vs}\Theta$.

The background state is unstable, and the unstable eigenmodes are used to create the initial conditions. In particular, we use a band of eigenmodes centered around the unstable wave vector $(k, l) = (3, 1)$, where the eigenmodes are obtained by solving the linearized equation for PV and M [15].

Parameter values of the "standard case" numerical simulation are listed in Table 1. The parameter values follow those used in [65] for the mid-latitude atmospheric case, except we are using smaller value of $U = 0.15$ to account for an extra factor of $(1+q^1_{vs})$ in PV background in order to have a more consistent jet in the standard case. To help see the connection with the parameters of [65], different parameters are listed in the tables of parameters, note the parameter relations $k_d^2 = 8 * (L/L_{du})^2$ and $L_{du}/L_{ds} = (1 + G_M)^{1/2}$; consequently our choice of $L/L_{ds} = 2.0$ matches the choice of $k_d = 4.0$ in [65].

Table 1: Standard Case Simulation Parameters

N	β	G_M	$\frac{L}{L_{ds}}$	U	κ	ν	Δz	q^1_{vs}	V_r	E
128	2.5	1.0	2.0	0.15	0.05	$5 * 10^{-15}$	0.5	1.0	1.0	0.02

The numerical scheme involves two parts. First, the evolution equations in (18) are advanced forward by one time step using a pseudospectral method for the spatial derivatives. The time-stepper is a 3rd-order Runge-Kutta scheme with an adaptive Δt chosen to satisfy the CFL condition. New values of PV_1, PV_2, and M_m are now known after advancing by one time step. Second, the new PV and M values are used to find the new values of all other variables, such as θ_e, u, v, etc. in a procedure called PV-and-M inversion. [These new values of θ_e, u, v, etc. are needed in order to take our next time step of (18)]. In terms of equations, PV-and-M inversion involves solving the elliptic PDE in (14a)–(14b). Notice that the elliptic PDE has variable coefficients, since the Heavisides H_u and H_s depend on x and y; as a result, Fourier spectral methods are less effective when phase changes are present. As an alternative, we use a conjugate gradient method to solve the elliptic PDE. Also, the elliptic PDE is nonlinear, since the Heavisides depend on q_t, and q_t depends on ψ, from (6)–(9). To handle the nonlinearity, a simple iterative method is used. See the appendix for further details of the numerical methods. Note that the algorithm here is meant to be simple and as close as possible to traditional algorithms for turbulence simulations [65,15], for ease of use. It would be interesting in the future to investigate more sophisticated methods. For instance, the elliptic solver used here is only first-order accurate, due to the PDE's discontinuous, variable coefficients; it would be interesting to design a more complex scheme that can achieve second-order accuracy for this nonlinear problem, possibly based on a second-order scheme for linear PDEs [56,58,3,9,57,75].

3 Numerical simulations of mid-latitude jets

How do phase changes influence QG turbulence? To investigate this question, a suite of numerical simulations is presented in this section.

The focus is on parameters that appear in moist QG but not in dry QG, including evaporation rate E, meridional moisture gradient Q_y, and rainfall speed V_r. As described in section 2, their standard values here are $E = 0.02, V_r = 1.0$, and $q_{vs}^1 = 1.0$ so that $Q_y = \Theta$, which will be the parameter values used unless otherwise specified.

3.1 Evaporation E and jet shifting

We begin by investigating simulations with different values of evaporation rate E. In addition to the dry case ($E = 0$) and the standard moist case $E = 0.02$, we also consider larger values of $E = 0.05$ and $E = 0.1$.

First consider the jet in each case, as shown in snapshots of zonal wind in Figure 2. In three cases, a single jet is present, and it is indicated by the large eastward ($u_2 > 0$) values that appear over a narrow range of latitudes and extend across all longitudes. For instance, in Figure 2c, the jet is mostly confined between $y = -2$ and $y = 0$. One difference between the dry case (Figure 2d) and the phase-change cases (Figure 2a,b,c) is that the phase-change cases appear to have more variability on small scales (which will be discussed further in a section about spectra and regularity below).

To better illustrate the effects of varying E values, Figure 3 displays the upper-level zonally-averaged wind as a function of time, from $t = 0$ to $t = 800$. In the dry case (Figure 3d) the jet remains near the same latitude for all times (in between roughly $y = 0$ and $= 1$). As E increases, there is a trend toward an increasing number of jets, and they propagate poleward. For example, for $E = 0.02$ shown in Figure 3c, there is a single zonally-averaged jet moving slightly northward. Moreover, the propagation speeds (represented by the lines in each plot) are faster for higher values of $E = 0.05, 0.1$ and the poleward trend is more apparent (Figure 3a,b).

Furthermore, different E values give rise to changes in total water and rainwater in the domain, as illustrated by Figures 4 and 5, which show snapshots of mid-level q_t and q_r, respectively. Recall that $q_t = q_v + q_r$. In Figure 4, rainwater is represented by positive values where areas are red. When $E = 0.02$ (Figure 4c), there is little rain, corresponding to Figure 5c and later on Figure 6c, and the negative value (q_v) indicated by blue areas gives a single jet. An increasing E value results in larger portion of red area in the snapshots of q_t as well as in the snapshots of q_r. The jet migration present in Figure 4c thus becomes less obvious in Figure 4a,b as discussed in previous paragraph regarding Figure 3.

Lastly, the impact of different E values is also demonstrated by time series of cloud fraction in each case. The cloud fraction $\overline{H_s}(t)$ is defined as the fraction

of the domain that is occupied by rainfall—i.e.,

$$\overline{H_s}(t) = \frac{1}{A} \int_A H_s(x, y, t)\, dx\, dy, \tag{19}$$

where A is the area of the domain and $H_s(x, y, t)$ is the Heaviside function that indicates a saturated region. It may be more appropriate to refer to $\overline{H_s}(t)$ as the rain fraction, since it is actually the fraction of the domain with rainfall present, as the simplified cloud microphysics scheme here has rainwater but not cloud liquid water per se [25]; nevertheless, we will use the term cloud fraction since it is used more commonly. As shown in Figure 6, a small $E = 0.02$ gives a relatively small cloud fraction mainly in the range between 0.02 and 0.06 (Figure 6c). As E becomes larger, higher cloud fractions are shown in Figure 6a,b. $E = 0.05$ gives a fraction ranging from 0.06 to 0.14. $E = 0.1$ gives a fraction ranging from 0.1 to 0.2. Eventually, a dry case has zero cloud fraction. Hence the cloud fraction is strongly influenced by the E values. In essence, evaporation E is the (prescribed) moisture source, and it is compensated by the (interactive) moisture sink from rainfall. The evaporation and rainfall reach a rough balance, the case of a larger evaporation rate will require a larger cloud fraction and more rainfall to maintain a statistical steady state.

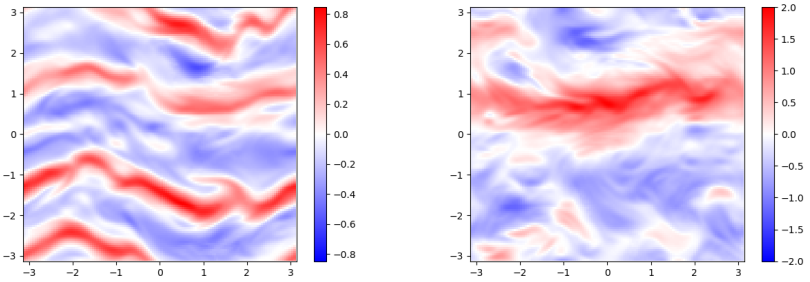

(a) $u_2(x, y)$ for $E = 0.1$ **(b)** $u_2(x, y)$ for $E = 0.05$

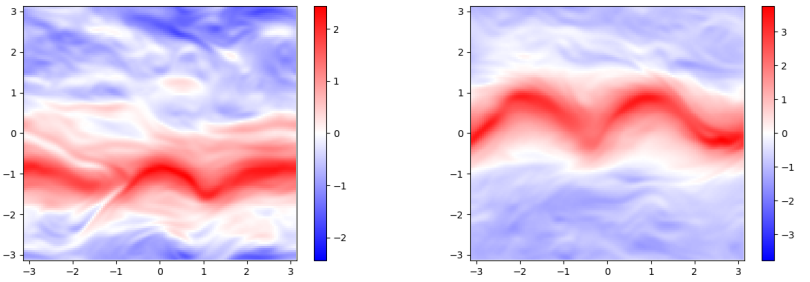

(c) $u_2(x, y)$ for $E = 0.02$ **(d)** $u_2(x, y)$ for dry case

Fig. 2 Snapshots of zonal velocity $u_2(x, y)$ at time $t = 640$. **(a,b,c)** $E = 0.1, 0.05, 0.02$, respectively. **(d)** The dry case without the phase change

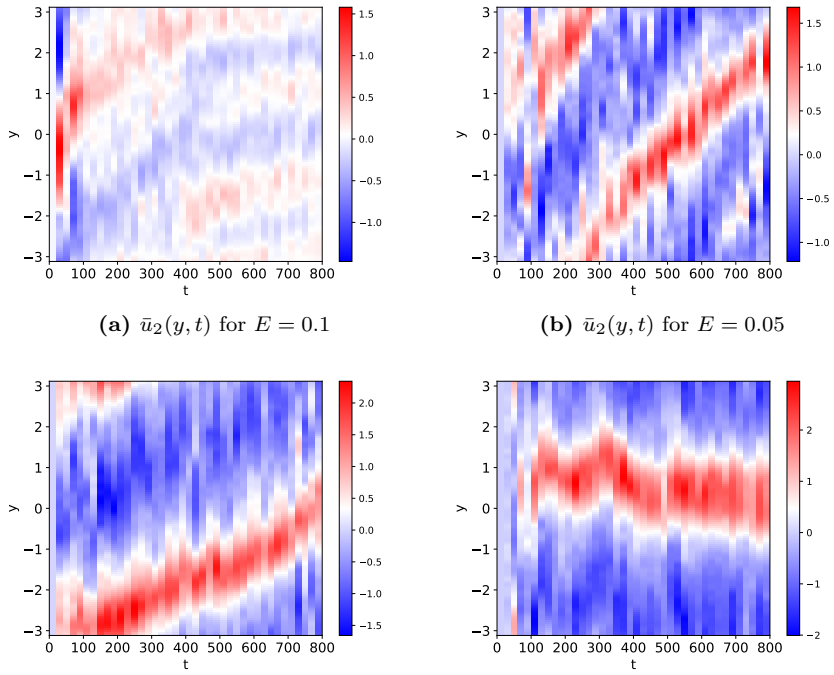

(a) $\bar{u}_2(y,t)$ for $E = 0.1$

(b) $\bar{u}_2(y,t)$ for $E = 0.05$

(c) $\bar{u}_2(y,t)$ for $E = 0.02$

(d) $\bar{u}_2(y,t)$ for dry case

Fig. 3 Poleward propagation of the jet, as indicated by the evolution of $\bar{u}_2(y,t)$, the zonally-averaged zonal wind at level 2. **(a,b,c)** $E = 0.1, 0.05, 0.02$, respectively. **(d)** The dry case without the phase change

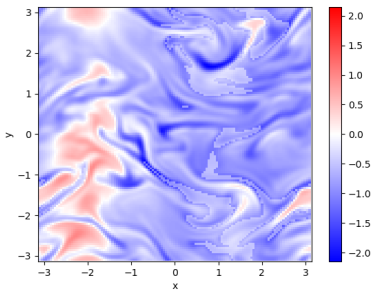

(a) $q_{t,m}(x, y)$ for $E = 0.1$

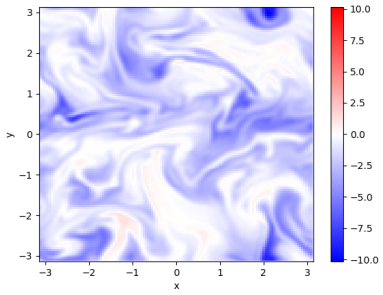

(b) $q_{t,m}(x, y)$ for $E = 0.05$

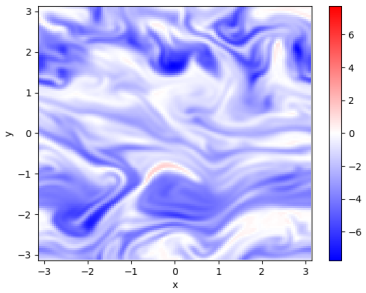

(c) $q_{t,m}(x, y)$ for $E = 0.02$

Fig. 4 Snapshots of total water, $q_{t,m}(x, t)$, at $t = 640$. **(a,b,c)** $E = 0.1, 0.05, 0.02$, respectively

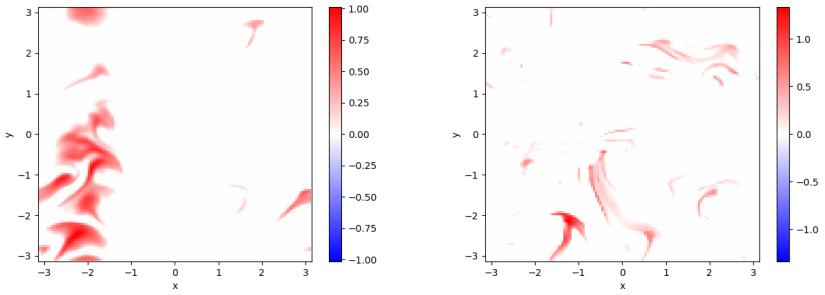

(a) $q_{r,m}(x, y)$ for $E = 0.1$

(b) $q_{r,m}(x, y)$ for $E = 0.05$

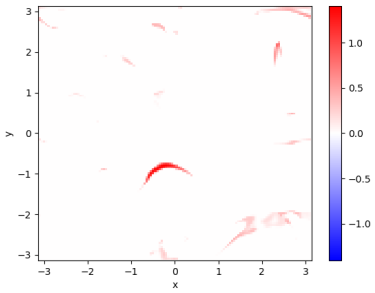

(c) $q_{r,m}(x, y)$ for $E = 0.02$

Fig. 5 Snapshots of rainwater, $q_{r,m}(x, t)$, at $t = 640$. **(a,b,c)** $E = 0.1, 0.05, 0.02$, respectively

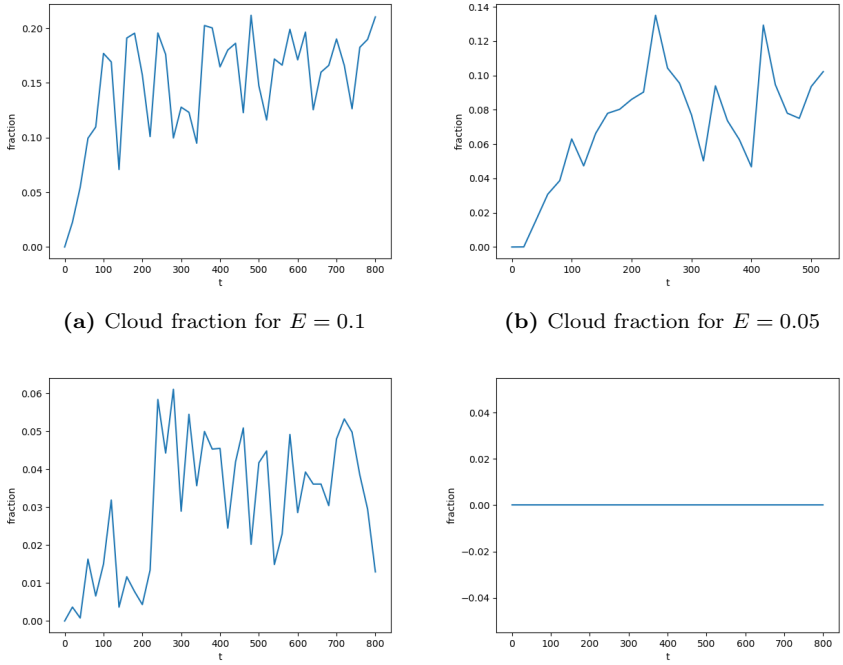

(a) Cloud fraction for $E = 0.1$

(b) Cloud fraction for $E = 0.05$

(c) Cloud fraction for $E = 0.02$

(d) Cloud fraction for dry case

Fig. 6 Time series of cloud fraction. **(a,b,c)** $E = 0.1, 0.05, 0.02$, respectively. **(d)** The dry case without the phase change

3.2 Meridional moisture gradient Q_y and temperature-dependence of q_{vs}

Recall the newly defined q_{vs} is different from its definition in [70]. Here $q_{vs} = q^0_{vs} + q^1_{vs}\theta$ where q^0_{vs} and q^1_{vs} are constant parameters mentioned in section 2. Moreover, recall the water gradient Q_y is tied to q^1_{vs} that $Q_y = q^1_{vs}\Theta$ for the purpose of maintaining a homogeneous setting. The simulations below shown in Figure 7 and Figure 8 have fixed evaporation value $E = 0.02$.

To see if changing q^1_{vs} promotes changes in jet shifting, Figure 7 shows plots of zonally averaged wind at upper level from $t = 0$ to $t = 800$. Figure 7a is when $q^1_{vs} = 0$ and two jets are presented and almost horizontal. As q^1_{vs} increases to 0.25 and 0.5, the trend of jets does not change. When q^1_{vs} is set to be 1.0, there is only one single jet that is present in Figure 7d. This is because the low cloud fraction shown in Figure 8d and somewhat similar to the jet behavior in dry case. Also notice the jet is moving slightly northward. Since the constant q^1_{vs} is related to meridional moisture gradient (Q_y), larger q^1_{vs} values correspond to larger Q_y values. Therefore, when Q_y increases, it appears to promote poleward propagation of the jet. It is reasonable to conclude that q^1_{vs} (or equivalently

Q_y) is another factor for the presence of poleward jet migration, in addition to E.

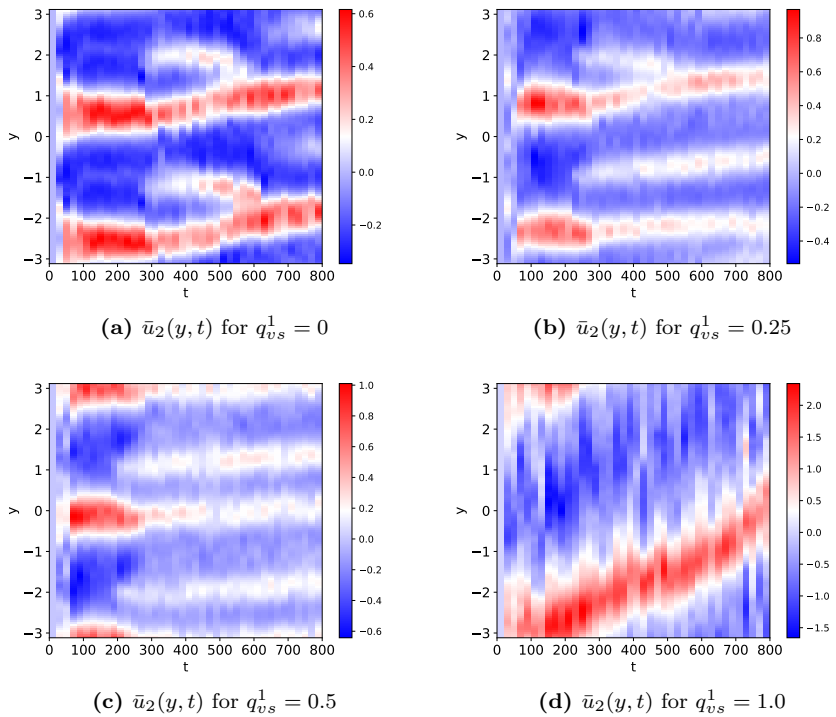

(a) $\bar{u}_2(y,t)$ for $q^1_{vs} = 0$

(b) $\bar{u}_2(y,t)$ for $q^1_{vs} = 0.25$

(c) $\bar{u}_2(y,t)$ for $q^1_{vs} = 0.5$

(d) $\bar{u}_2(y,t)$ for $q^1_{vs} = 1.0$

Fig. 7 Propagation of the jet, as indicated by $\bar{u}_2(y,t)$, the zonally-averaged zonal wind at level 2. **(a,b,c,d)** $q^1_{vs} = 0, 0.25, 0.5, 1.0$, respectively

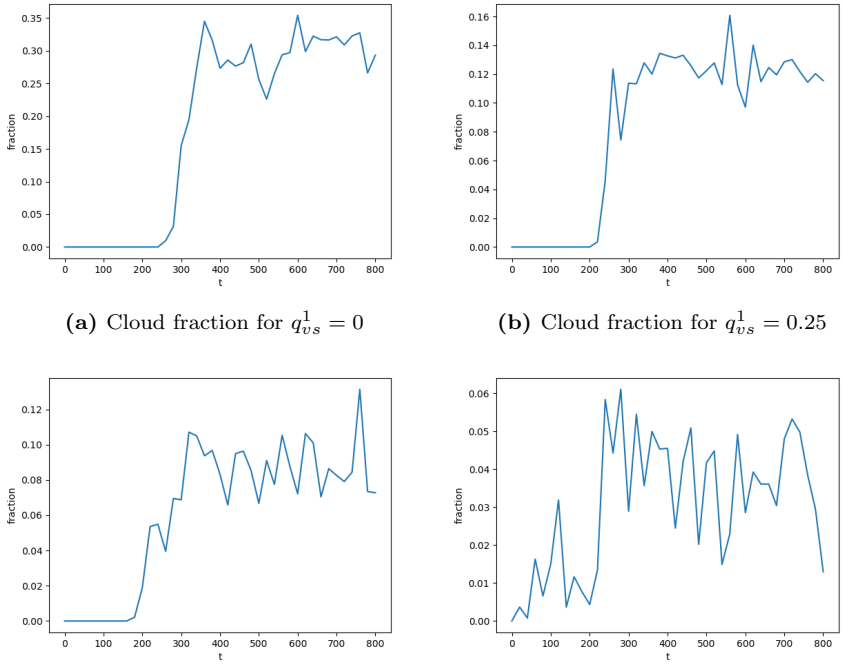

(a) Cloud fraction for $q^1_{vs} = 0$

(b) Cloud fraction for $q^1_{vs} = 0.25$

(c) Cloud fraction for $q^1_{vs} = 0.5$

(d) Cloud fraction for $q^1_{vs} = 1.0$

Fig. 8 Time series of cloud fraction. **(a,b,c,d)** $q^1_{vs} = 0, 0.25, 0.5, 1.0$, respectively

3.3 Rainfall speed V_r

To encapsulate the effects of varying rainfall speed V_r, different from other cases where $V_r = 1.0$, Figure 9a,b are plots of cloud fraction for $V_r = 0.25$ and $V_r = 4.0$ respectively. Figure 9c,d are plots of zonally averaged wind at upper level for $V_r = 0.25$ and $V_r = 4.0$ respectively when $E = 0.02$. As V_r is decreased by four times, the cloud fraction has slightly larger values for most of the time in Figure 9a comparing to Figure 6c. On the other hand, as V_r is increased by four times, the cloud fraction is almost 0 for majority of the time (Figure 9b). Nonetheless, the jet formulations of $\bar{u}_2$ do not change drastically in Figure 9d comparing to Figure 3c since the cloud fractions of both cases are similar. Yet, in Figure 9c, where cloud fraction has increased, there is faster speed of jet propagation as seen in previous high cloud fraction cases demonstrated by Figure 3a,b.

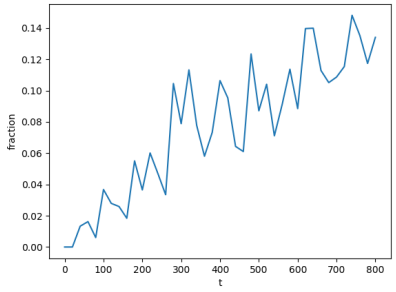

(a) Cloud fraction for $V_r = 0.25, E = 0.02$

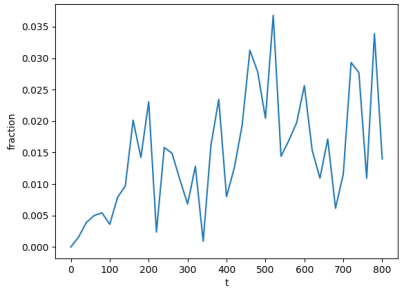

(b) Cloud fraction for $V_r = 4.0, E = 0.02$

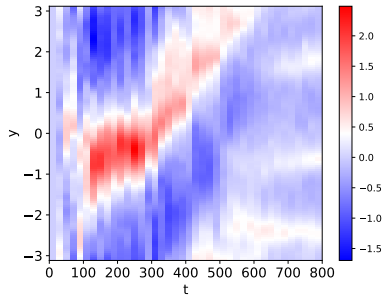

(c) $\bar{u}_2(y,t)$ for $V_r = 0.25, E = 0.02$

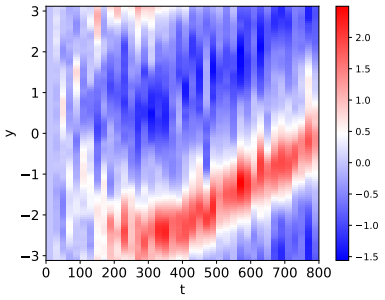

(d) $\bar{u}_2(y,t)$ for $V_r = 4.0, E = 0.02$

Fig. 9 Comparison of $V_r = 0.25$ (left column) and 4.0 (right column). **(a-b)** Time series of cloud fraction for $V_r = 0.25$ and 4.0 respectively. **(c-d)** Evolution of $\bar{u}_2(y,t)$, the zonally averaged zonal wind at level 2, for $V_r = 0.25$ and 4.0 respectively

3.4 Spectra and regularity

Given that the PQG equations involve phase changes and Heaviside nonlinearities, it is interesting to explore the regularity of solutions in the numerical simulations. To investigate regularity, Figure 10 shows spectra for several important variables: $PV_2, M_m, \theta_{e,m}$ and $q_{t,m}$. Notice that PV and M appear to have smoother spectra, which is likely because they are explicitly evolved and influenced directly by hyperviscosity (Figure 10a,b). On the other hand, the other variables are obtained at least partially from the streamfunction ψ, which is obtained from after solving the nonlinear elliptic PDE which has the discontinuous coefficients due to the phase change introduced by Heaviside functions. Consequently, taking the derivative of ψ will potentially create a loss of smoothness/regularity at the phase interface for variables such as θ_e (Figure 10c) and for other variables that come from ψ such as u, v, q_t (Figure 10d).

An indication of the smoothness/regularity can also be seen visually in the snapshots in Figure 2. The dry case (Figure 2d) does not appear to have as much variability as the phase change cases (Figure 2a,b,c). This series of snapshots shows that u_2, which is obtained after the inversion step, is more irregular in phase change case due to the existence of discontinuous coefficient in PV equations. This serves to illustrate some of the challenges involved in numerical simulations with the combined effects of both turbulence and phase changes.

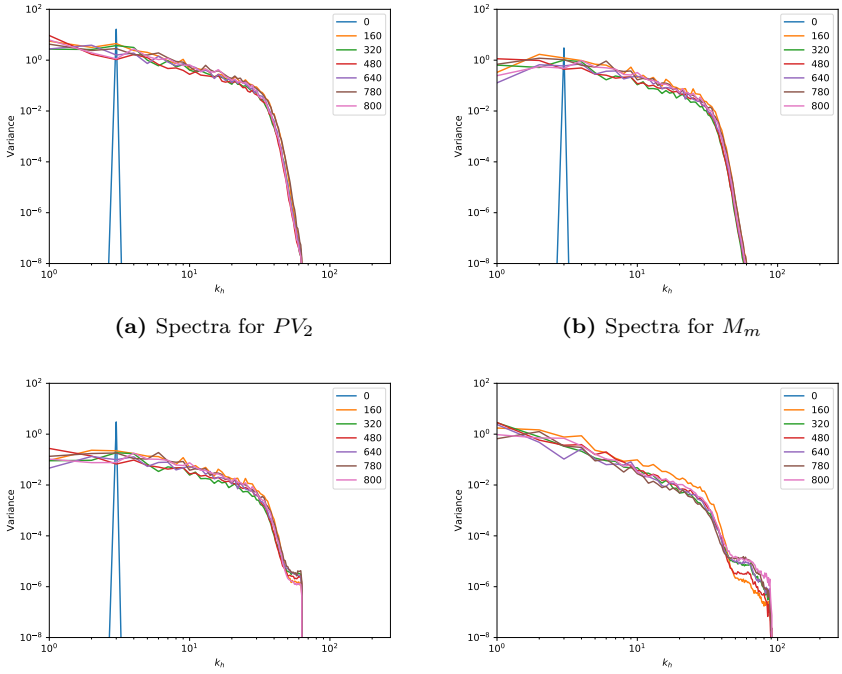

(a) Spectra for PV_2

(b) Spectra for M_m

(c) Spectra for $\theta_{e,m}$

(d) Spectra for $q_{t,m}$

Fig. 10 Spectra plots—i.e., variance as a function of wavenumber. Different curves are shown for different times. **(a,b,c,d)** $PV_2, M_m, \theta_{e,m}$ and $q_{t,m}$, respectively

3.5 Higher resolution sensitivity studies

To ensure that higher resolution simulations present similar phenomena of jet shifting, plots of zonally averaged wind at upper level and snapshots of zonal wind at different times with resolution $N = 256$ are shown in Figure 11b,d,f. The case shown in Figure 11 uses the standard parameter values from Table 1 (aside from using $N = 128$ in the left column and $N = 256$ in the right

column of Figure 11). Notice that, in the high-resolution simulation in Figure 11b, the jet does also move poleward, indicating that jet shifting occurs in simulations at different resolutions. In other details, though, the low-resolution (Figure 11a) and higher resolution (Figure 11b) show some differences, such as a longer spin-up time until roughly $t = 500$ or 600 before the jet shifting begins in the higher resolution simulation. To show more detail of the jets, snapshots of the jets are shown from Figure 11(c) to Figure 11(e) at times $t = 80$ and $t = 240$. Given that these are snapshots from turbulent simulations, one cannot expect agreement of detailed features between the $N = 128$ and $N = 256$ cases, but this comparison does show that the jets in the $N = 128$ and $N = 256$ cases have somewhat similar variations. Overall, this comparison indicates that some details differ in these turbulent simulations at different resolutions, but the basic phenomenon of jet shifting also appears in higher resolution simulations.

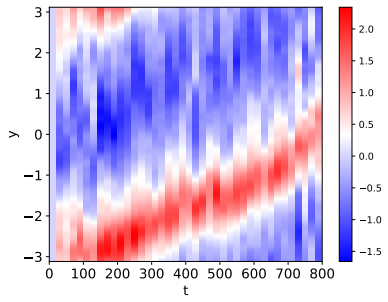

(a) $\bar{u}_2(y,t)$ for $N = 128$

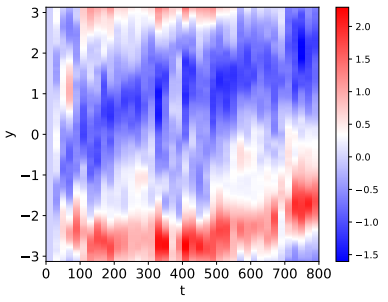

(b) $\bar{u}_2(y,t)$ for $N = 256$

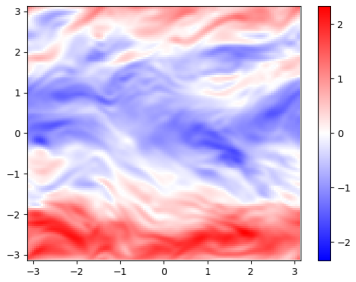

(c) $u_2(x,y)$ for $N = 128$ at $t = 80$

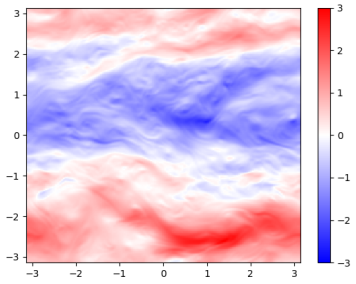

(d) $u_2(x,y)$ for $N = 256$ at $t = 80$

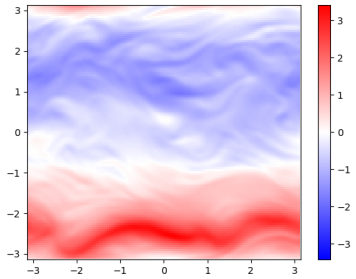

(e) $u_2(x,y)$ for $N = 128$ at $t = 240$

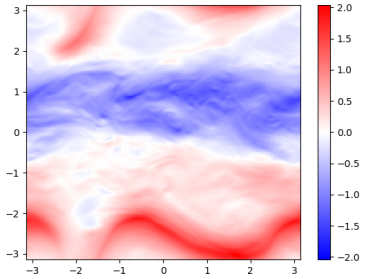

(f) $u_2(x,y)$ for $N = 256$ at $t = 240$

Fig. 11 Comparison of standard resolution ($N = 128$, left column) and a higher resolution simulation ($N = 256$, right column). **(a,b)** Zonally-averaged zonal velocity at level 2, $\bar{u}_2(y,t)$. **(c,d)** Snapshots of $u_2(x,y)$ at $t = 80$. **(e,f)** Snapshots of $u_2(x,y)$ at $t = 240$

4 Concluding discussion

A setup of QG turbulence was presented here to include the effects of rainfall and phase changes. Precipitating QG turbulence presents numerous challenges

(in terms of mathematics, computation, and physical understanding) due to the combined influence of turbulence and phase changes. A two-level setup was described as the simplest setup with these effects, and it includes an associated energy principle. A numerical method was also presented, including an iterative method for the solution of the nonlinear elliptic PDE for PV-and-M inversion. For the dynamical evolution equations, standard pseudospectral methods were used in order to remain as close as possible to traditional numerical methods for turbulent fluid dynamics. In an initial exploration of numerical simulations, one new feature that arises due to phase changes is the poleward propagation of the jet.

The simulations suggest some interesting behavior for future study from the point of view of geophysical fluid dynamics. It would be interesting to further explore, for instance, the idea of an effective static stability for geostrophic turbulence with phase changes [59]. It would also be interesting to explore the poleward propagation of the jets that was seen in the simulations here. While the precise mechanisms are perhaps not the same, propagation or movement or shifting of jets has also been a topic of interest for the jet streams in nature. For instance, one question is whether or not (and if so then via what mechanisms) the jet streams are shifting poleward in latitude due to global warming [33,68,42]. Another interesting topic is the occasional superposition of the subtropical and polar jets [81,8], which tends to be in localized regions and can be associated with extreme weather events.

The PQG equations also suggest further mathematical questions of PDE analysis. The regularity of solutions to the PQG equations (both the nonlinear elliptic PDE for PV-and-M inversion as well as the full dynamical evolution equations) remains an open question. It would also be interesting to further explore the discontinuous front solutions [78], and, for instance, their stability.

5 Appendix: Energetics

To derive the energy principle in (15)–(16), it is convenient to note the following form of the evolution equations:

$$\frac{D_i \zeta_i}{Dt} + \beta v_i = (-1)^{i-1} \frac{w}{\Delta z}, \quad \text{for } i = 1, 2, \tag{20a}$$

$$\frac{D_m b_u}{Dt} + w \frac{L_{du}}{L} = \frac{-V_r}{\Delta z} q_r, \tag{20b}$$

$$\frac{D_m b_s}{Dt} + w \frac{L_{ds}}{L_{du}} \frac{L_{ds}}{L} = 0, \tag{20c}$$

where w, b_u, b_s, and q_r are from the middle height, from Fig. 1, but their subscripts m have been suppressed to ease notation. These are the two-level version of (1). Note that the equations for θ_e and q_t have been rewritten in terms of the buoyancy variables b_u and b_s, as in the appendix of [70]; however, a typo in (A14b) of [70], in the coefficient of w, has been corrected here.

Also useful are the relations for geostrophic and hydrostatic balance from (6), written in terms of b_u and b_s as

$$\mathbf{u}_h = \nabla_h^{\perp}\psi, \quad b_u H_u + b_s H_s = \frac{L}{L_{du}}\frac{\partial \psi}{\partial z}. \tag{21}$$

The derivations of the energy transfers in (16) are as follows. Note the relations $(d/dt)\int_A F dA = \int_A (\partial F/\partial t) dA = \int_A (D_h F/Dt) dA$ are used to take derivatives with respect to time.

For the kinetic energy, by equation (20a) and $\zeta = \nabla_h^2 \psi$,

$$\begin{aligned}
\frac{d}{dt}KE &= \frac{1}{2}\frac{d}{dt}\int_A \nabla_h\psi_1 \cdot \nabla_h\psi_1 + \nabla_h\psi_2 \cdot \nabla_h\psi_2 \, dA \\
&= -\frac{1}{2}\frac{d}{dt}\int_A \psi_1\zeta_1 + \psi_2\zeta_2 \, dA \\
&= -\frac{1}{2}\int_A \psi_1\frac{\mathrm{D}_1\zeta_1}{\mathrm{D}t} + \psi_2\frac{\mathrm{D}_2\zeta_2}{\mathrm{D}t} + \zeta_1\frac{\mathrm{D}_1\psi_1}{\mathrm{D}t} + \zeta_2\frac{\mathrm{D}_2\psi_2}{\mathrm{D}t} \, dA \\
&= -\frac{1}{2}\int_A \psi_1\frac{\mathrm{D}_1\zeta_1}{\mathrm{D}t} + \psi_2\frac{\mathrm{D}_2\zeta_2}{\mathrm{D}t} + \zeta_1\frac{\partial\psi_1}{\partial t} + \zeta_2\frac{\partial\psi_2}{\partial t} \, dA \\
&= -\frac{1}{2}\int_A \psi_1\frac{\mathrm{D}_1\zeta_1}{\mathrm{D}t} + \psi_2\frac{\mathrm{D}_2\zeta_2}{\mathrm{D}t} - \nabla_h\psi_1 \cdot \nabla_h\frac{\partial\psi_1}{\partial t} - \nabla_h\psi_2 \cdot \nabla_h\frac{\partial\psi_2}{\partial t} \, dA \\
&= \frac{1}{2}\frac{d}{dt}KE - \frac{1}{2}\int_A \psi_1\frac{\mathrm{D}_h\zeta_1}{\mathrm{D}t} + \psi_2\frac{\mathrm{D}_h\zeta_2}{\mathrm{D}t} \, dA \\
&= \frac{1}{2}\frac{d}{dt}KE - \frac{1}{2}\int_A \frac{w}{\Delta z}(\psi_1 - \psi_2) - \psi_1\beta\frac{\partial\psi_1}{\partial x} - \psi_2\beta\frac{\partial\psi_2}{\partial x} \, dA \\
&= \frac{1}{2}\frac{d}{dt}KE + \frac{1}{2}\int_A w\frac{\psi_2 - \psi_1}{\Delta z} \, dA.
\end{aligned} \tag{22}$$

In the calculation, integration by parts was used, along with doubly periodic boundary conditions. Also used was the relation $\mathbf{u}_h \cdot \nabla_h \psi = 0$, which follows from the definition $\mathbf{u}_h = \nabla_h^{\perp}\psi$ and is valid at each vertical level. Note that the Coriolis term, βv_i, does not make any contribution to the energy.

For the unsaturated potential energy, by equation (20b) and equation (21),

$$\begin{aligned}
\frac{d}{dt}PE_u &= \frac{1}{2}\frac{d}{dt}\int_A H_u\frac{L^2}{L_{du}^2}\left(\frac{\psi_2 - \psi_1}{\Delta z}\right)^2 \, dA \\
&= \frac{1}{2}\frac{d}{dt}\int_A H_u b_u^2 \, dA \\
&= \frac{1}{2}\int_A \frac{\mathrm{D}_h H_u}{\mathrm{D}t} b_u^2 \, dA + \int_A H_u b_u \frac{\mathrm{D}_h b_u}{\mathrm{D}t} \, dA \\
&= -\frac{1}{2}\int_A \frac{\mathrm{D}_h H_s}{\mathrm{D}t} b_u^2 \, dA - \int_A H_u b_u \left(w\frac{L_{du}}{L} + \frac{V_r}{\Delta z}q_r\right) dA \\
&= -\frac{1}{2}\int_A \frac{\mathrm{D}_h H_s}{\mathrm{D}t}\frac{L^2}{L_{du}^2}\frac{(\psi_2 - \psi_1)^2}{(\Delta z)^2} \, dA - \int_A H_u w\frac{\psi_2 - \psi_1}{\Delta z} \, dA.
\end{aligned} \tag{23}$$

The V_r term disappears because $q_r H_u$ is 0.

For the saturated potential energy, by equation (20c) and equation (21),

$$\begin{aligned}
\frac{d}{dt}PE_s &= \frac{1}{2}\frac{d}{dt}\int_A H_s \frac{L^2}{L_{ds}^2}\left(\frac{\psi_2-\psi_1}{\Delta z}\right)^2 dA \\
&= \frac{1}{2}\frac{d}{dt}\int_A H_s \frac{L_{du}^2}{L_{ds}^2} b_s^2\, dA \\
&= \frac{1}{2}\int_A \frac{\mathrm{D}_h H_s}{\mathrm{D}t}\frac{L_{du}^2}{L_{ds}^2} b_s^2\, dA + \int_A H_s \frac{L_{du}^2}{L_{ds}^2} b_s \frac{\mathrm{D}_h b_s}{\mathrm{D}t}\, dA \\
&= \frac{1}{2}\int_A \frac{\mathrm{D}_h H_s}{\mathrm{D}t}\frac{L_{du}^2}{L_{ds}^2} b_s^2\, dA - \int_A H_s \frac{L_{du}^2}{L_{ds}^2} b_s (w\frac{L_{ds}}{L_{du}}\frac{L_{ds}}{L})\, dA \\
&= \frac{1}{2}\int_A \frac{\mathrm{D}_h H_s}{\mathrm{D}t}\frac{L^2}{L_{ds}^2}\frac{(\psi_2-\psi_1)^2}{(\Delta z)^2}\, dA - \int_A H_s w \frac{\psi_2-\psi_1}{\Delta z}\, dA.
\end{aligned} \tag{24}$$

For the moist energy, starting from (15) and using (13) and (6), we find

$$\begin{aligned}
\frac{d}{dt}ME &= \frac{1}{2G_M}\frac{d}{dt}\int_A H_u\left(M - \frac{L_{du}^2}{L_{ds}^2}q_{vs}\right)^2 dA, \\
&= \frac{1}{G_M}\int_A \frac{1}{2}\frac{\mathrm{D}_h H_u}{\mathrm{D}t}\left(M - \frac{L_{du}^2}{L_{ds}^2}q_{vs}\right)^2 + H_u\frac{1}{2}\frac{\mathrm{D}_h}{\mathrm{D}t}\left(M - \frac{L_{du}^2}{L_{ds}^2}q_{vs}\right)^2 dA, \\
&= \frac{1}{G_M}\int_A \frac{1}{2}\frac{\mathrm{D}_h H_u}{\mathrm{D}t}\left(q_t + G_M\theta_e - \frac{L_{du}^2}{L_{ds}^2}q_{vs}\right)^2 \\
&\qquad - H_u\left(M - \frac{L_{du}^2}{L_{ds}^2}q_{vs}\right)\frac{V_r}{\Delta z}q_r dA, \\
&= \frac{1}{G_M}\int_A \frac{1}{2}\frac{\mathrm{D}_h H_u}{\mathrm{D}t}\left(q_t + G_M(\theta+q_v) - \frac{L_{du}^2}{L_{ds}^2}q_{vs}\right)^2 dA, \\
&= \frac{1}{G_M}\int_A \frac{1}{2}\frac{\mathrm{D}_h H_u}{\mathrm{D}t}\left(q_{vs} + G_M(\theta+q_{vs}) - \frac{L_{du}^2}{L_{ds}^2}q_{vs}\right)^2 dA, \\
&= \int_A \frac{1}{2}\frac{\mathrm{D}_h H_u}{\mathrm{D}t} G_M\theta^2 dA, \\
&= \frac{1}{2}\int_A \frac{\mathrm{D}_h H_s}{\mathrm{D}t}\frac{(\psi_2-\psi_1)^2}{(\Delta z)^2}\left(\frac{L^2}{L_{du}^2} - \frac{L^2}{L_{ds}^2}\right) dA.
\end{aligned} \tag{25}$$

In the calculation above, notice that $D_h H_u/Dt$ is a Dirac delta function at the phase interface; consequently, in the coefficient of $D_h H_u/Dt$, one can replace q_t by q_{vs} since $q_t - q_{vs} = 0$ at the phase interface. The V_r term disappears because $q_r H_u$ is 0. Note that the only term remaining in $(d/dt)ME$ is a Dirac delta term at the phase interface, so the moist energy (ME) transfer only happens at phase interface. This completes the derivation of the energy transfers in (16).

6 Appendix: Numerical methods

In this appendix, some aspects of the numerical methods are described in further detail. This includes, first, the iterative method that is used for solving the nonlinear elliptic PDE, and, second, an outline of one time step of the numerical method. The outline is as follows, and the elliptic PDE solver is described as the first stage.

1) After evolving the PV and M variables according to their evolution equations in (18), the next task is to perform PV-and-M inversion by solving the nonlinear elliptic PDE in (14a)–(14b), which we rewrite here for convenience:

$$\begin{aligned} PV_{e,1} = \nabla_h^2 \psi_1 &+ H_s \left(\left(\frac{L}{L_{ds}} \frac{1}{\Delta z} \right)^2 (\psi_2 - \psi_1) + \frac{L_{du}}{L_{ds}} \frac{L}{L_{ds}} \frac{1}{\Delta z} q_{vs,m} \right) \\ &+ H_u \left(\left(\frac{L}{L_{du}} \frac{1}{\Delta z} \right)^2 (\psi_2 - \psi_1) + \frac{L}{L_{du}} \frac{1}{\Delta z} M_m \right) \end{aligned} \tag{26}$$

$$\begin{aligned} PV_{e,2} = \nabla_h^2 \psi_2 &+ H_s \left(\left(\frac{L}{L_{ds}} \frac{1}{\Delta z} \right)^2 (\psi_1 - \psi_2) - \frac{L_{du}}{L_{ds}} \frac{L}{L_{ds}} \frac{1}{\Delta z} q_{vs,m} \right) \\ &+ H_u \left(\left(\frac{L}{L_{du}} \frac{1}{\Delta z} \right)^2 (\psi_1 - \psi_2) - \frac{L}{L_{du}} \frac{1}{\Delta z} M_m \right) \end{aligned} \tag{27}$$

Recall that this elliptic PDE is nonlinear because the Heaviside functions H_u and H_s are functions of q_t, which itself is found from M and ψ_z.

To solve the nonlinear elliptic PDE, an iterative method is used, as follows. In the first iteration, initial guesses $H_u^{[1]}(x,y)$ and $H_s^{[1]}(x,y)$ are used for the Heavisides, and the elliptic PDE is solved as a linear PDE with $H_u^{[1]}(x,y)$ and $H_s^{[1]}(x,y)$ frozen. As a good choice for the initial guesses $H_u^{[1]}(x,y)$ and $H_s^{[1]}(x,y)$ for the Heavisides, one can use the values of the Heavisides H_u and H_s from the previous time step. Standard centered differences were used to discretize the PDE, even though the PDE has discontinuous coefficients, so that the method is somewhat similar in spirit to the ghost fluid method [40,41]. A conjugate gradient method was used to solve the discretized linear system of equations for $\psi^{[1]}$. Given the solution $\psi^{[1]}$, one can calculate new estimates $H_u^{[2]}(x,y)$ and $H_s^{[2]}(x,y)$ for the Heavisides. To do so, we use $\psi^{[1]}$ and M to calculate $q_t^{[1]}$, as described further below, and then $H_u^{[2]}(x,y)$ and $H_s^{[2]}(x,y)$ are defined based on $q_t^{[1]}$. Given the new estimates $H_u^{[2]}(x,y)$ and $H_s^{[2]}(x,y)$ for the Heavisides, the iterative method can be continued to determine a new streamfunction estimate $\psi^{[2]}$, etc. The iterations stop when the new Heavisides $H_u^{[k+1]}(x,y)$ and $H_s^{[k+1]}(x,y)$ are the same as the previous Heavisides $H_u^{[k]}(x,y)$ and $H_s^{[k]}(x,y)$, since the same streamfunctions $\psi^{[k]}$ and $\psi^{[k+1]}$ would then also be the same. We conducted offline convergence tests of this numerical method, and we also analyzed it in time-evolving simulations. In the time-evolving simulations, the number of iterations required was always fewer than

10 and typically ranging from 2 to 4. As a result, the elliptic solver is more computationally expensive than in the case without phase changes, although the difference in expense is not too great.

The main output of this stage is then the updated value of streamfunction ψ at the new time step.

2) Compute $\frac{\partial \psi}{\partial z}$ at the middle level of the domain, for use in defining the thermodynamic variables (θ_e, q_t, q_{vs}, q_r):

$$\left.\frac{\partial \psi}{\partial z}\right|_m = \frac{1}{\Delta z}(\psi_2 - \psi_1) \tag{28}$$

(29)

3) Compute new q_{vs} based on $\frac{\partial \psi}{\partial z}$:

$$q_{vs} = q_{vs}^0 + q_{vs}^1 \left.\frac{\partial \psi}{\partial z}\right|_m \tag{30}$$

4) Compute $\theta_{e,m}$ and $q_{t,m}$ using (14c) and (14d); e.g.,

$$q_t = M - G_M \theta_e - q_{vs}. \tag{31}$$

5) Compute q_r at the middle level:

$$q_r = \max(0, M - G_M \theta_e - q_{vs}) \tag{32}$$

6) Update the Heaviside functions based on

$$H_s(x,y) = \begin{cases} 0 & \text{if } q_r(x,y) = 0 \\ 1 & \text{if } q_r(x,y) > 0 \end{cases} \tag{33}$$

$$H_u(x,y) = \begin{cases} 0 & \text{if } q_r(x,y) > 0 \\ 1 & \text{if } q_r(x,y) = 0 \end{cases} \tag{34}$$

7) Obtain rainfall forcing on the right hand side of M equation and E is the evaporation term:

$$forcing = \frac{V_r}{\Delta z} q_r + E \tag{35}$$

8) This stage and the following stages are used to compute the velocity $\mathbf{u}_h$ and the terms $(\partial \mathbf{u}_h / \partial z) \cdot \nabla_h \theta_e$ that appear in the PV evolution equations.

Obtain ψ_3, ψ_0 (values of streamfunction at ghost levels outside the model domain) by using the boundary conditions $\psi_z = 0$, which follow from the boundary conditions that θ_e and M are zero on top and bottom. Explicitly, the values are then defined as

$$\psi_3 = \psi_2 \tag{36}$$

$$\psi_0 = \psi_1 \tag{37}$$

9) Obtain $\frac{\partial \psi}{\partial z}$ at level 2, level 1 as

$$\left.\frac{\partial \psi}{\partial z}\right|_2 = \frac{1}{\Delta z}\frac{\psi_3 - \psi_1}{2} \tag{38}$$

$$\left.\frac{\partial \psi}{\partial z}\right|_1 = \frac{1}{\Delta z}\frac{\psi_2 - \psi_0}{2} \tag{39}$$

10) Take horizontal derivatives of ψ_1, ψ_2, $\psi_z|_1$, and $\psi_z|_2$ to obtain u, v, and $\frac{\partial u_h}{\partial z}$ at levels 1 and 2 for the PV evolution equation.

11) Given $\theta_{e,m}$ from above, and also using the boundary values of $\theta_{e,t}$ and $\theta_{e,b}$ (which were set to zero here), obtain

$$\theta_{e,2} = \frac{1}{2}(\theta_{e,t} + \theta_{e,m}) \tag{40}$$

$$\theta_{e,1} = \frac{1}{2}(\theta_{e,m} + \theta_{e,b}) \tag{41}$$

which are the final components needed to compute the terms $(\partial \mathbf{u}_h/\partial z) \cdot \nabla_h \theta_e$ that appear in the PV evolution equations, at level 1 and level 2.

12) Step forward in time with the evolution equations from (18)

13) Go back to 1)

Acknowledgements This research is partially supported by grant NSF DMS–1907667.

Conflict of interest

The authors have no conflict of interest to declare.

References

1. Abramov, R.V., Majda, A.J.: Statistically relevant conserved quantities for truncated quasigeostrophic flow. Proceedings of the National Academy of Sciences **100**(7), 3841–3846 (2003)
2. Abramov, R.V., Majda, A.J.: Low-frequency climate response of quasigeostrophic wind-driven ocean circulation. Journal of Physical Oceanography **42**(2), 243–260 (2012)
3. Bedrossian, J., Von Brecht, J.H., Zhu, S., Sifakis, E., Teran, J.M.: A second order virtual node method for elliptic problems with interfaces and irregular domains. J. Comput. Phys. **229**(18), 6405–6426 (2010)
4. Betts, A.K.: A new convective adjustment scheme. Part I: Observational and theoretical basis. Q. J. Roy. Met. Soc. **112**, 677–692 (1986)
5. Charney, J.G.: The dynamics of long waves in a baroclinic westerly current. J. Meteorol. **4**(5), 136–162 (1947)
6. Charney, J.G.: On the scale of atmospheric motions. Geofys. Publ. Oslo **17**(2), 1–17 (1948)
7. Charney, J.G.: Geostrophic turbulence. J. Atmos. Sci. **28**(6), 1087–1095 (1971)
8. Christenson, C.E., Martin, J.E., Handlos, Z.J.: A synoptic climatology of northern hemisphere, cold season polar and subtropical jet superposition events. Journal of Climate **30**(18), 7231–7246 (2017)

9. Crockett, R.K., Colella, P., Graves, D.T.: A cartesian grid embedded boundary method for solving the poisson and heat equations with discontinuous coefficients in three dimensions. J. Comput. Phys. **230**(7), 2451–2469 (2011)
10. Deng, Q., Smith, L.M., Majda, A.J.: Tropical cyclogenesis and vertical shear in a moist Boussinesq model. J. Fluid Mech. **706**, 384–412 (2012)
11. Dutrifoy, A., Majda, A.: The dynamics of equatorial long waves: a singular limit with fast variable coefficients. Commun. Math. Sci. **4**(2), 375–397 (2006)
12. Dutrifoy, A., Majda, A.: Fast wave averaging for the equatorial shallow water equations. Communications in Partial Differential Equations **32**, 1617–1642 (2007)
13. Dutrifoy, A., Majda, A.J., Schochet, S.: A simple justification of the singular limit for equatorial shallow-water dynamics. Communications on Pure and Applied Mathematics **62**(3), 322–333 (2009)
14. Edwards, T.K., Smith, L.M., Stechmann, S.N.: Atmospheric rivers and water fluxes in precipitating quasi-geostrophic turbulence. Quarterly Journal of the Royal Meteorological Society p. in press (2020). DOI 10.1002/qj.3777
15. Edwards, T.K., Smith, L.M., Stechmann, S.N.: Spectra of atmospheric water in precipitating quasi-geostrophic turbulence. Geophysical & Astrophysical Fluid Dynamics p. in press (2020). DOI 10.1080/03091929.2019.1692205
16. Emanuel, K.A., Fantini, M., Thorpe, A.J.: Baroclinic instability in an environment of small stability to slantwise moist convection. Part I: Two-dimensional models. J. Atmos. Sci. **44**(12), 1559–1573 (1987)
17. Embid, P.F., Majda, A.J.: Averaging over fast gravity waves for geophysical flows with arbitary potential vorticity. Comm. PDEs **21**(3-4), 619–658 (1996)
18. Embid, P.F., Majda, A.J.: Low Froude number limiting dynamics for stably stratified flow with small or finite Rossby numbers. Geophys. Astrophys. Fluid Dynam. **87**(1-2), 1–50 (1998)
19. Frierson, D.M.W., Held, I.M., Zurita-Gotor, P.: A gray-radiation aquaplanet moist GCM. Part I: Static stability and eddy scale. J. Atmos. Sci. **63**(10), 2548–2566 (2006)
20. Frierson, D.M.W., Majda, A.J., Pauluis, O.M.: Large scale dynamics of precipitation fronts in the tropical atmosphere: a novel relaxation limit. Commun. Math. Sci. **2**(4), 591–626 (2004)
21. Grooms, I., Lee, Y., Majda, A.J.: Numerical schemes for stochastic backscatter in the inverse cascade of quasigeostrophic turbulence. Multiscale Modeling & Simulation **13**(3), 1001–1021 (2015)
22. Grooms, I., Majda, A.J.: Efficient stochastic superparameterization for geophysical turbulence. Proc. Natl. Acad. Sci. USA **110**, 4464–4469 (2013)
23. Grooms, I., Majda, A.J.: Stochastic superparameterization in quasigeostrophic turbulence. Journal of Computational Physics **271**, 78–98 (2014)
24. Grooms, I., Majda, A.J., Smith, K.S.: Stochastic superparameterization in a quasigeostrophic model of the antarctic circumpolar current. Ocean Modelling **85**, 1–15 (2015)
25. Hernandez-Duenas, G., Majda, A.J., Smith, L.M., Stechmann, S.N.: Minimal models for precipitating turbulent convection. J. Fluid Mech. **717**, 576–611 (2013). DOI 10.1017/jfm.2012.597
26. Hernandez-Duenas, G., Smith, L.M., Stechmann, S.N.: Stability and instability criteria for idealized precipitating hydrodynamics. J. Atmos. Sci. **72**(6), 2379–2393 (2015). DOI 10.1175/JAS-D-14-0317.1
27. Kalnay, E.: Atmospheric modeling, data assimilation and predictability. Cambridge University Press (2003)
28. Khouider, B., Majda, A.J.: A non-oscillatory balanced scheme for an idealized tropical climate model: Part I: Algorithm and validation. Theor. Comp. Fluid Dyn. **19**(5), 331–354 (2005)
29. Khouider, B., Majda, A.J.: A non-oscillatory balanced scheme for an idealized tropical climate model: Part II: Nonlinear coupling and moisture effects. Theor. Comp. Fluid Dyn. **19**(5), 355–375 (2005)
30. Khouider, B., Majda, A.J.: Multicloud convective parameterizations with crude vertical structure. Theor. Comp. Fluid Dyn. **20**, 351–375 (2006)
31. Khouider, B., Majda, A.J.: A simple multicloud parameterization for convectively coupled tropical waves. Part I: Linear analysis. J. Atmos. Sci. **63**, 1308–1323 (2006)

32. Khouider, B., Majda, A.J., Stechmann, S.N.: Climate science in the tropics: waves, vortices and PDEs. Nonlinearity **26**(1), R1–R68 (2013)
33. Kidston, J., Gerber, E.: Intermodel variability of the poleward shift of the austral jet stream in the cmip3 integrations linked to biases in 20th century climatology. Geophysical Research Letters **37**(9) (2010)
34. Klainerman, S., Majda, A.: Singular limits of quasilinear hyperbolic systems with large parameters and the incompressible limit of compressible fluids. Comm. Pure Appl. Math. **34**(4), 481–524 (1981)
35. Klainerman, S., Majda, A.: Compressible and incompressible fluids. Comm. Pure Appl. Math. **35**(5), 629–651 (1982)
36. Klein, R., Majda, A.: Systematic multiscale models for deep convection on mesoscales. Theor. Comp. Fluid Dyn. **20**, 525–551 (2006)
37. Laîné, A., Lapeyre, G., Rivière, G.: A quasigeostrophic model for moist storm tracks. Journal of the atmospheric sciences **68**(6), 1306–1322 (2011)
38. Lapeyre, G., Held, I.M.: The role of moisture in the dynamics and energetics of turbulent baroclinic eddies. J. Atmos. Sci. **61**(14), 1693–1710 (2004)
39. Lee, Y., Majda, A., Qi, D.: Preventing catastrophic filter divergence using adaptive additive inflation for baroclinic turbulence. Mon. Wea. Rev. **145**(2), 669–682 (2017). DOI 10.1175/MWR-D-16-0121.1
40. Liu, X.D., Fedkiw, R.P., Kang, M.: A boundary condition capturing method for Poisson's equation on irregular domains. J. Comput. Phys. **160**(1), 151–178 (2000)
41. Liu, X.D., Sideris, T.: Convergence of the ghost fluid method for elliptic equations with interfaces. Math. Comput. **72**(244), 1731–1746 (2003)
42. Maher, P., Kelleher, M.E., Sansom, P.G., Methven, J.: Is the subtropical jet shifting poleward? Climate Dynamics **54**(3), 1741–1759 (2020)
43. Majda, A.: Compressible Fluid Flow and Systems of Conservation Laws in Several Space Variables, *Applied Mathematical Sciences*, vol. 53. Springer-Verlag, New York (1984)
44. Majda, A., Wang, X.: Validity of the one and one-half layer quasi-geostrophic model and effective topography. Communications in Partial Differential Equations **30**(9), 1305–1314 (2005)
45. Majda, A., Wang, X.: Nonlinear dynamics and statistical theories for basic geophysical flows. Cambridge University Press (2006)
46. Majda, A.J.: Introduction to PDEs and Waves for the Atmosphere and Ocean, *Courant Lecture Notes in Mathematics*, vol. 9. American Mathematical Society, Providence (2003)
47. Majda, A.J., Embid, P.: Averaging over fast gravity waves for geophysical flows with unbalanced initial data. Theor. Comput. Fluid Dyn. **11**(3-4), 155–169 (1998)
48. Majda, A.J., Klein, R.: Systematic multiscale models for the Tropics. J. Atmos. Sci. **60**, 393–408 (2003)
49. Majda, A.J., Mohammadian, M., Xing, Y.: Vertically sheared horizontal flow with mass sources: a canonical balanced model. Geophys. Astrophys. Fluid Dynam. **102**(6), 543–591 (2008)
50. Majda, A.J., Qi, D.: Strategies for reduced-order models for predicting the statistical responses and uncertainty quantification in complex turbulent dynamical systems. SIAM Review **60**(3), 491–549 (2018)
51. Majda, A.J., Souganidis, P.E.: Existence and uniqueness of weak solutions for precipitation fronts: A novel hyperbolic free boundary problem in several space variables. Comm. Pure Appl. Math. **63**(10), 1351–1361 (2010)
52. Majda, A.J., Stechmann, S.N.: The skeleton of tropical intraseasonal oscillations. Proc. Natl. Acad. Sci. USA **106**(21), 8417–8422 (2009)
53. Majda, A.J., Wang, X.: The emergence of large-scale coherent structure under small-scale random bombardments. Communications on Pure and Applied Mathematics **59**(4), 467–500 (2006)
54. Majda, A.J., Xing, Y., Mohammadian, M.: Moist multi-scale models for the hurricane embryo. J. Fluid Mech. **657**, 478–501 (2010)
55. Marsico, D.H., Smith, L.M., Stechmann, S.N.: Energy decompositions for moist Boussinesq and anelastic equations with phase changes. Journal of the Atmospheric Sciences p. in press (2019). DOI 10.1175/JAS-D-19-0080.1

56. Oevermann, M., Klein, R.: A cartesian grid finite volume method for elliptic equations with variable coefficients and embedded interfaces. Journal of Computational Physics **219**(2), 749–769 (2006)
57. Oevermann, M., Klein, R.: An asymptotic solution approach for elliptic equations with discontinuous coefficients. Journal of Computational Physics **261**, 230–243 (2014)
58. Oevermann, M., Scharfenberg, C., Klein, R.: A sharp interface finite volume method for elliptic equations on cartesian grids. Journal of Computational Physics **228**(14), 5184–5206 (2009)
59. O'Gorman, P.A.: The effective static stability experienced by eddies in a moist atmosphere. J. Atmos. Sci. **68**(1), 75–90 (2011)
60. Opsteegh, J., Haarsma, R., Selten, F., Kattenberg, A.: ECBILT: A dynamic alternative to mixed boundary conditions in ocean models. Tellus A: Dynamic Meteorology and Oceanography **50**(3), 348–367 (1998)
61. Pauluis, O., Balaji, V., Held, I.M.: Frictional dissipation in a precipitating atmosphere. J. Atmos. Sci. **57**(7), 989–994 (2000)
62. Pauluis, O., Dias, J.: Satellite estimates of precipitation-induced dissipation in the atmosphere. Science **335**(6071), 953–956 (2012). DOI 10.1126/science.1215869
63. Pedlosky, J.: Geophysical Fluid Dynamics, 2nd edn. Springer–Verlag (1987)
64. Phillips, N.A.: Energy transformations and meridional circulations associated with simple baroclinic waves in a two-level, quasi-geostrophic model. Tellus **6**(3), 273–286 (1954)
65. Qi, D., Majda, A.J.: Low-dimensional reduced-order models for statistical response and uncertainty quantification: Two-layer baroclinic turbulence. Journal of the Atmospheric Sciences **73**(12), 4609–4639 (2016)
66. Qi, D., Majda, A.J.: Predicting extreme events for passive scalar turbulence in two-layer ba roclinic flows through reduced-order stochastic models. Communications in Mathematical Sciences **16**(1), 17–51 (2018)
67. Rhines, P.B.: Geostrophic turbulence. Ann. Rev. Fluid Mech. **11**(1), 401–441 (1979)
68. Rivière, G.: A dynamical interpretation of the poleward shift of the jet streams in global warming scenarios. Journal of the Atmospheric Sciences **68**(6), 1253–1272 (2011)
69. Salmon, R.: Baroclinic instability and geostrophic turbulence. Geophys. Astro. Fluid **15**(1), 167–211 (1980)
70. Smith, L.M., Stechmann, S.N.: Precipitating quasigeostrophic equations and potential vorticity inversion with phase changes. J. Atmos. Sci. **74**, 3285–3303 (2017). DOI 10.1175/JAS-D-17-0023.1
71. Stechmann, S.N., Majda, A.J.: The structure of precipitation fronts for finite relaxation time. Theor. Comp. Fluid Dyn. **20**, 377–404 (2006)
72. Thompson, A.F., Young, W.R.: Two-layer baroclinic eddy heat fluxes: Zonal flows and energy balance. J. Atmos. Sci. **64**(9), 3214–3231 (2007)
73. Tulloch, R., Smith, K.S.: A note on the numerical representation of surface dynamics in quasigeostrophic turbulence: Application to the nonlinear eady model. Journal of the atmospheric sciences **66**(4), 1063–1068 (2009)
74. Tulloch, R., Smith, K.S.: Quasigeostrophic turbulence with explicit surface dynamics: Application to the atmospheric energy spectrum. Journal of the atmospheric sciences **66**(2), 450–467 (2009)
75. Tzou, C.N., Stechmann, S.N.: Simple second-order finite differences for elliptic PDEs with discontinuous coefficients and interfaces. Comm. App. Math. and Comp. Sci. **14**, 121–147 (2019). DOI 10.2140/camcos.2019.14.121
76. Vallis, G.: Atmospheric and Oceanic Fluid Dynamics: Fundamentals and Large-scale Circulation. Cambridge University Press, New York (2006)
77. Wetzel, A.N., Smith, L.M., Stechmann, S.N.: Moisture transport due to baroclinic waves: Linear analysis of precipitating quasi-geostrophic dynamics. Math. Clim. Weather Forecast. **3**(1), 28–50 (2017). DOI 10.1515/mcwf-2017-0002
78. Wetzel, A.N., Smith, L.M., Stechmann, S.N.: Discontinuous fronts as exact solutions to precipitating quasi-geostrophic equations. SIAM J. Appl. Math. **79**, 1341–1366 (2019). DOI 10.1137/18M119478
79. Wetzel, A.N., Smith, L.M., Stechmann, S.N., Martin, J.E.: Balanced and unbalanced components of moist atmospheric flows with phase changes. Chin. Ann. Math. Ser. B **40**, 1005–1038 (2019). DOI 10.1007/s11401-019-0170-4

80. Wetzel, A.N., Smith, L.M., Stechmann, S.N., Martin, J.E., Zhang, Y.: Potential vorticity and balanced and unbalanced moisture. J. Atmos. Sci. **77**, 1913–1931 (2020). DOI 10.1175/JAS-D-19-0311.1
81. Winters, A.C., Martin, J.E.: Synoptic and mesoscale processes supporting vertical superposition of the polar and subtropical jets in two contrasting cases. Quarterly Journal of the Royal Meteorological Society **142**(695), 1133–1149 (2016)